Angewandte Chemie International Edition

Angewandte International Edition Chemie

How to cite: *Angew. Chem. Int. Ed.* **2026**, e6558145
doi.org/10.1002/anie.6558145

RESEARCH ARTICLE Hot Paper

Dual-Affinity Interphase Engineering Enables Stable Aqueous Zn–S Batteries

Zeheng Lv[1] | Peiyao Wang[1] | Sirui Lin[1] | Xinran Li[2] | Ruibo Sun[1] | Kaiwen Li[1] | Hong Lin[1] | Fanxiang Meng[1] | Minghao Zhang[1] | Yang Yang[1] | Hao Luo[3] | Jinbao Zhao[1] | Dongliang Chao[2]

[1]State Key Laboratory of Physical Chemistry of Solid Surfaces, State-Province Joint Engineering Laboratory of Power Source Technology for New Energy Vehicle, College of Chemistry and Chemical Engineering, Xiamen University, Xiamen, P. R. China | [2]Laboratory of Advanced Materials, Shanghai Key Laboratory of Molecular Catalysis and Innovative Materials, College of Smart Materials and Future Energy, Fudan University, Shanghai, P. R. China | [3]School of Materials Science and Engineering, Xiamen University of Technology, Xiamen, P. R. China

Correspondence: Yang Yang (yangyang419@xmu.edu.cn) | Hao Luo (luohao@xmut.edu.cn) | Dongliang Chao (chaod@fudan.edu.cn)

Received: 22 March 2026 | **Revised:** 29 May 2026 | **Accepted:** 4 June 2026

Keywords: aqueous Zn–S batteries | Cu CEI | dual-affinity interphase | S_8 ring opening | ZnS stabilization

ABSTRACT

Aqueous Zn–S batteries have garnered significant attention for grid-scale storage but suffer from rapid capacity fade and sluggish reaction kinetics. Although existing strategies can improve redox reversibility, they fail to fundamentally address capacity attenuation arising from oxidation-driven ZnS decomposition loss. In this study, a nano-copper-based cathode/electrolyte interphase (Cu CEI) featuring a unique sulfur/ZnS dual-affinity is rationally designed to accelerate both S—S and Zn—S bond dynamics, effectively preventing ZnS accumulation and suppressing its decomposition via preferential Cu-ZnS binding. Specifically, the strong binding affinity of the Cu CEI stabilizes ZnS by reducing its direct contact with interfacial water. Meanwhile, the strong interaction between Cu nanoparticles and S_8 activates ring-opening and facilitates S—S bond cleavage, elevating the discharge voltage to 0.75 V. Cu-mediated weakening of Zn—S bonds in ZnS synergistically lowers the apparent activation energy from 69.4 to 29.5 kJ mol^{-1}, establishing a robust interfacial redox pathway with a low voltage hysteresis of 0.23 V. Consequently, the Cu CEI enables Zn–S system with excellent cycling stability over 1000 cycles at 5 A g^{-1} and a high areal capacity of ~6.5 mAh cm^{-2} over 200 h in a pouch cell, underscoring the practical feasibility of this dual-affinity interphase design for high-performance Zn–S batteries.

1 | Introduction

As a low-cost and environmentally benign conversion-type cathode [1–3], sulfur (S) undergoes a one-step solid-to-solid (STS) conversion mechanism between S and ZnS in aqueous Zn–S battery systems [4]. This reaction pathway inherently avoids the shuttling of soluble sulfur intermediates, which drives rapid capacity decay in Li-S batteries using organic electrolytes, while simultaneously offering an ultrahigh theoretical capacity of 1675 mAh g^{-1} [5–12]. However, during repeated cycling, the intrinsically high bond dissociation energies of S—S bonds in S_8 and Zn—S bonds in ZnS impose substantial energetic penalties for their continuous cleavage and reformation. Meanwhile, the rapid capacity fade also presents a major challenge to the cycling stability of Zn–S batteries. In addition, the pronounced volumetric mismatch between S and ZnS induces irreversible structural deformation of sulfur particles [13–18], further aggravating polarization and accelerating capacity fading [19–21]. Therefore, simultaneously accelerating conversion kinetics and suppressing capacity decay is essential for developing high-performance aqueous Zn–S batteries.

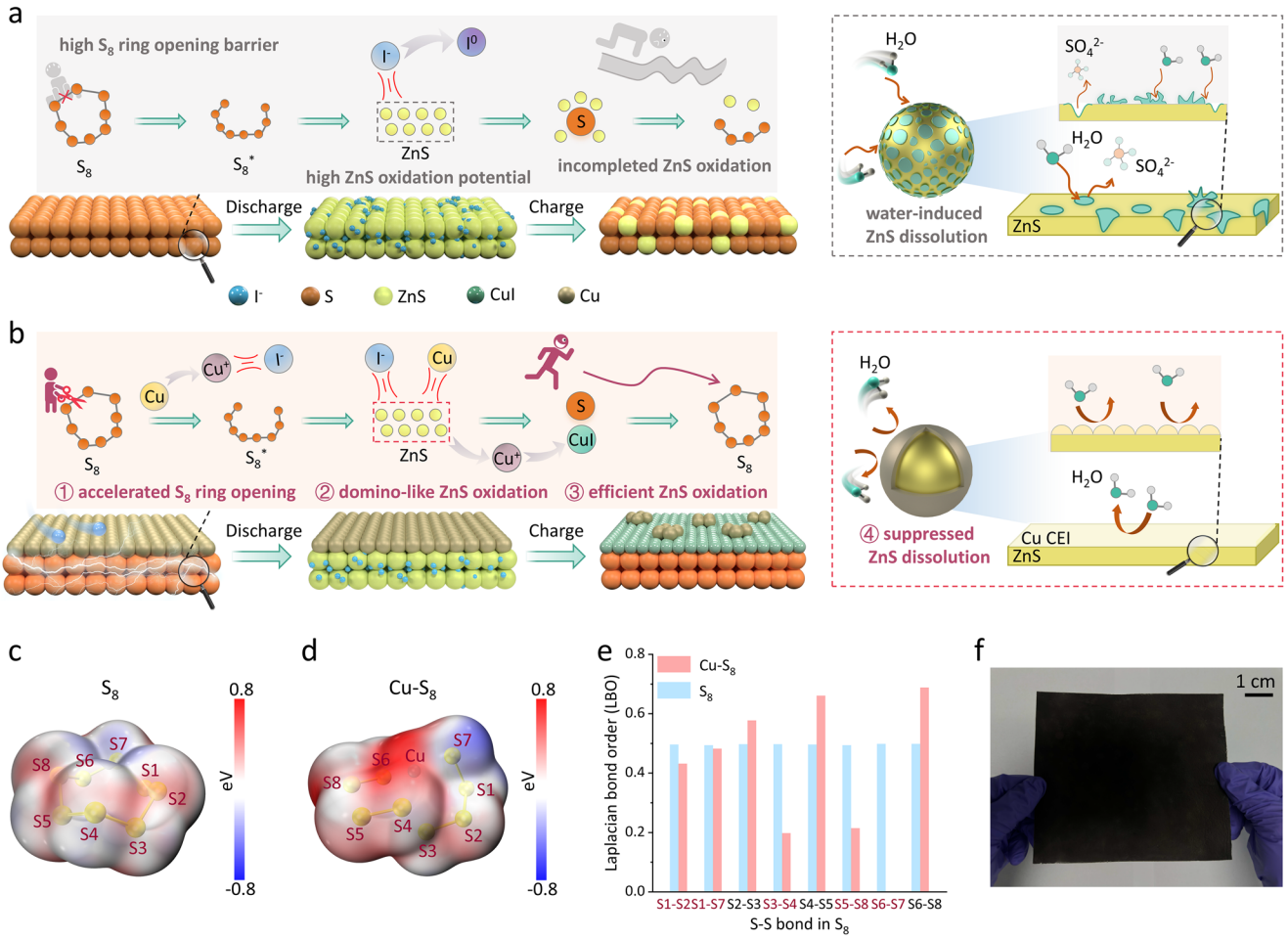

FIGURE 1 | Proposed mechanism of Cu CEI in Zn–S batteries. Schematic illustrations of the redox process for Zn–S battery with (a) I^- and (b) Cu CEI, and the Cu CEI-mediated suppression of SO_4^{2-} formation. Electrostatic potential (ESP) distributions for (c) S_8 and (d) Cu-S_8. (e) Laplacian bond order (LBO) statistics for S_8 and Cu-S_8. (f) Photograph of the as-prepared Cu CEI.

Current research efforts primarily aim to overcome the sluggish ZnS↔S conversion by employing catalyst or redox-mediator engineering [22–26], electrolyte optimization [22, 27–29], and electrostatic mediation strategies [4, 30, 31]. Among these, iodide-based redox mediation (I^-) is the most widely adopted. This strategy requires charging to a relatively high potential (>1.2 V vs. Zn/Zn^{2+}) to oxidize I^- to I^0 [32], which subsequently promotes ZnS oxidation (Figure 1a). Nevertheless, this mediation process contributes little to sulfur reduction during discharge, thereby requiring a high charge cut-off voltage and resulting in a low average output voltage and compromised energy efficiency. Alternatively, the development of cosolvents (e.g., propylene glycol methyl ether; *N*,*N*-diethylformamide) is demonstrated to facilitate the reduction of S_8 to ZnS during discharge [29, 33]. However, achieving simultaneous enhancement of both charge and discharge kinetics within a limited operating voltage window remains highly challenging, originating from the insufficient ability of existing strategies to directly regulate the strong S—S and Zn—S bonds at the atomic scale. In particular, the large activation barrier associated with the initial S_8 ring-opening imposes unavoidable kinetic and mass-transport constraints. The stable crown-shaped S_8 molecules exhibit extremely low electronic conductivity ($\sim 5 \times 10^{-28}$ S cm^{-1}) due to poor electron delocalization [29, 31], while the high S—S bond dissociation energy (~169.5 kJ mol^{-1}) [34] further hinders both electron transfer and S_8 ring-opening during discharge, collectively limiting the practical voltage output of Zn–S batteries. Beyond kinetic limitations, the chemical instability of ZnS in aqueous environments represents another often-overlooked challenge. ZnS is susceptible to H_2O/O_2-induced corrosion at the cathode/electrolyte interface [35, 36], as well as electrochemically driven oxidation during charging, causing its conversion into soluble sulfate species (Equation 1). This irreversible process results in pronounced active-material loss and rapid capacity decay, particularly severe at high areal loadings and under moderate-rate conditions (e.g., 1 A g^{-1}), where prolonged exposure of large quantities of ZnS to the electrolyte accelerates cumulative SO_4^{2-} leaching (Figure 1a). Therefore, developing a tandem strategy that (i) directly modulates S—S and Zn—S bond dynamics to accelerate both charge and discharge kinetics, thereby mitigating ZnS accumulation, and (ii) stabilizes ZnS against aqueous corrosion to fundamentally suppress its decomposition, is essential for realizing high-areal-capacity aqueous Zn–S batteries with low voltage polarization and long-term cycling stability at practical low cycling rates.

$$2ZnS\,(s) + 4H_2O\,(l) - 10e^- \rightarrow S\,(s) + 2Zn^{2+}\,(aq) + SO_4^{2-}\,(aq) + 8H^+\,(aq) \quad (1)$$

In this work, a homogeneous artificial nano-copper-based cathode/electrolyte interphase (Cu CEI) layer with sulfur/ZnS dual-affinity was constructed to enable fast and reversible conversion kinetics (Figure 1b,f). The substantially stronger binding energy of Cu-ZnS (−3.25 eV), compared with that of H_2O-ZnS (−0.46 eV) indicates preferential ZnS interaction with the Cu CEI rather than with active water molecules, effectively suppressing both water-induced ZnS decomposition and the loss of forming soluble SO_4^{2-} species. Moreover, the significant adsorption affinity of Cu CEI for both S_8 and ZnS not only promotes S_8 ring-opening and reduction, but also triggers a domino-like ZnS oxidation, as detailed in the following section. Accordingly, the Cu CEI lowers the activation energy of the Zn–S system from 69.4 to 29.5 kJ mol^{-1}. Benefiting from the accelerated redox kinetics, the Zn–S battery exhibits a low voltage hysteresis of only 0.23 V and a high average discharge voltage of 0.75 V at 0.5 A g^{-1}. The Zn–S coin-type full cell with the Cu CEI demonstrates a markedly enhanced cycling stability, maintaining performance over 1000 cycles at 5 A g^{-1}. Furthermore, a corresponding Cu CEI-based Zn–S pouch cell delivers a high areal capacity of ∼6.5 mAh cm^{-2} for more than 200 h at 0.1 A g^{-1}, highlighting its strong potential for practical applications.

2 | Results and Discussion

2.1 | Failure Mechanisms Analysis in Aqueous Zn–S Batteries

To evaluate the electrochemical characteristics and capacity-decay mechanisms of aqueous Zn–S batteries, coin cells comprising a Zn anode and a S@C composite cathode (Figures S1–S3) were assembled as benchmark systems. As shown in Figure 2a, the S@C electrode delivers an initial discharge capacity of approximately 1500 mAh g^{-1} at 0.5 A g^{-1}, corresponding to ∼90% of the theoretical capacity based on the S^0/S^{2-} redox couple (1675 mAh g^{-1}). In sharp contrast, in the absence of a ZnI_2 mediator, the accumulation of insulating ZnS renders the sulfur electrode electrochemically inert (Figure S4). These results confirm that the presence of I^- species in the electrolyte is beneficial for promoting the electrochemical oxidation of ZnS (Figures S5 and S6) [23]. Despite this mediation effect, the S cathode still suffers from severe capacity fading upon stepwise increases in current density from 0.5 to 5 A g^{-1} (Figures 2b and S7). More critically, when the current density is reverted to 0.5 A g^{-1}, the capacity recovers to merely ∼500 mAh g^{-1}, far below its initial value. This pronounced irreversible capacity loss highlights the intrinsically poor rate capability of Zn–S batteries and is consistent with observations reported in prior studies [19, 22, 23, 29, 31, 37, 38].

Density functional theory (DFT) calculations provide mechanistic insight into this degradation behavior, revealing that oxygen atoms from active water molecules can directly attack Zn—S bonds in ZnS (Figure 2c; Figures S8–S10), thereby oxidizing active sulfur into soluble sulfate species (SO_4^{2-}). In contrast, the weak interaction between H_2O and S_8 suggests that direct water-induced activation of S_8 is unlikely to be the dominant origin of active sulfur dissolution (Figure S11). Experimentally, ion chromatography (IC) analysis of the Zn||S@C cell employing a glass-fiber (GF) separator in zinc acetate electrolyte shows a relatively enhanced SO_4^{2-} signal (∼6.75–7.67 μS) during discharge (Figure 2d), which is already higher than the baseline value of 4.77 μS obtained from the pristine sulfur cathode (Figure S12). This observation indicates spontaneous ZnS decomposition driven by the combined effects of water and dissolved oxygen. Notably, during charging, the SO_4^{2-} signal increases continuously from 12.34 μS at 1.2 V to 25.41 μS at 1.6 V, demonstrating that ZnS decomposition is strongly coupled with electrochemical oxidation. In contrast, after introducing a Cu CEI consisting of a nano-copper layer uniformly coated on the surface of glass fiber (Cu@GF, Figures S13–S18), the SO_4^{2-} intensity is effectively maintained at a low level of 4.64–5.58 μS during discharge (Figures 2e and S19). Upon charging, it increases only moderately from 7.09 μS at 0.7 V to 9.51 μS at 1.1 V, clearly indicating that the Cu CEI significantly stabilizes ZnS and suppresses sulfur/electrolyte interfacial side reactions. Quantitative analysis further reveals that, in the GF-based cell, a sulfur molar loss rate of approximately 29.4% (the generation of ∼6.89 mg L^{-1} SO_4^{2-} per milligram of sulfur) occurs after full charging (Figure 2f; Figures S20 and S21). This sulfur loss directly accounts for the irreversible capacity decay of the Zn–S battery and originates from the gradual migration of sulfur species out of the carbon host during prolonged cycling. Consistent with this interpretation, electrochemical impedance spectroscopy (EIS) reveals an increase in the electronic resistance of the cycled sulfur electrode (Figure 2g), possibly reflecting the electronic conductivity degradation caused by the leakage of insulating sulfur away from the conductive carbon framework. Further evidence is provided by in situ XRD (x-ray diffraction): during cycling, the diffraction signal of sulfur increases markedly, particularly near 25°, where a growing sulfur peak progressively overwhelms the broad carbon background (Figure 2h). This behavior indicates continuous sulfur recrystallization, attributable to sulfur migration and surface reorganization on the carbon host (Figure 2j). Thermodynamically, this process is driven by the strong tendency of S^{2-} to migrate toward the electrode surface and precipitate as ZnS upon reaction with Zn^{2+} (Equation 2), which weakens sulfur-carbon interactions and exacerbates corrosion-induced active-material loss in aqueous environments.

$$S^{2-}(aq) + Zn^{2+}(aq) \rightarrow ZnS(s)\ \Delta G = -139.87\ \text{kJ mol}^{-1} < 0 \quad (2)$$

$$S(s) + 2Cu(s) \rightarrow Cu_2S(s)\ \Delta G = -86.19\ \text{kJ mol}^{-1} < 0 \quad (3)$$

When the Cu@GF separator is employed, the attenuation of the carbon background near 25° proceeds much more slowly, and sulfur-related diffraction peaks in the 30°–40° range emerge only at later stages (Figure 2i). This phenomenon confirms that the Cu CEI strongly adsorbs sulfur species and modulates the polarity of crystalline S_8 (Figure 1c,d), likely driven by the spontaneous reaction between Cu and S (Equation 3), thereby suppressing sulfur leaching. Correspondingly, the reduced laplacian bond order (LBO) of most S—S bonds in the Cu-S_8 system reflects Cu-induced electronic modulation and suggests weakened S—S bonding, as well as a decrease in S—S bond dissociation energy (Figure 1e) [39], thereby facilitating S_8 ring opening and electrochemical reduction. This interpretation is supported by the original LBO study, which demonstrated that LBO is correlated with bond polarity, bond dissociation energy, and bond vibrational frequency, supporting its use as a quantitative descriptor of covalent bond strength. Although sulfur migra-

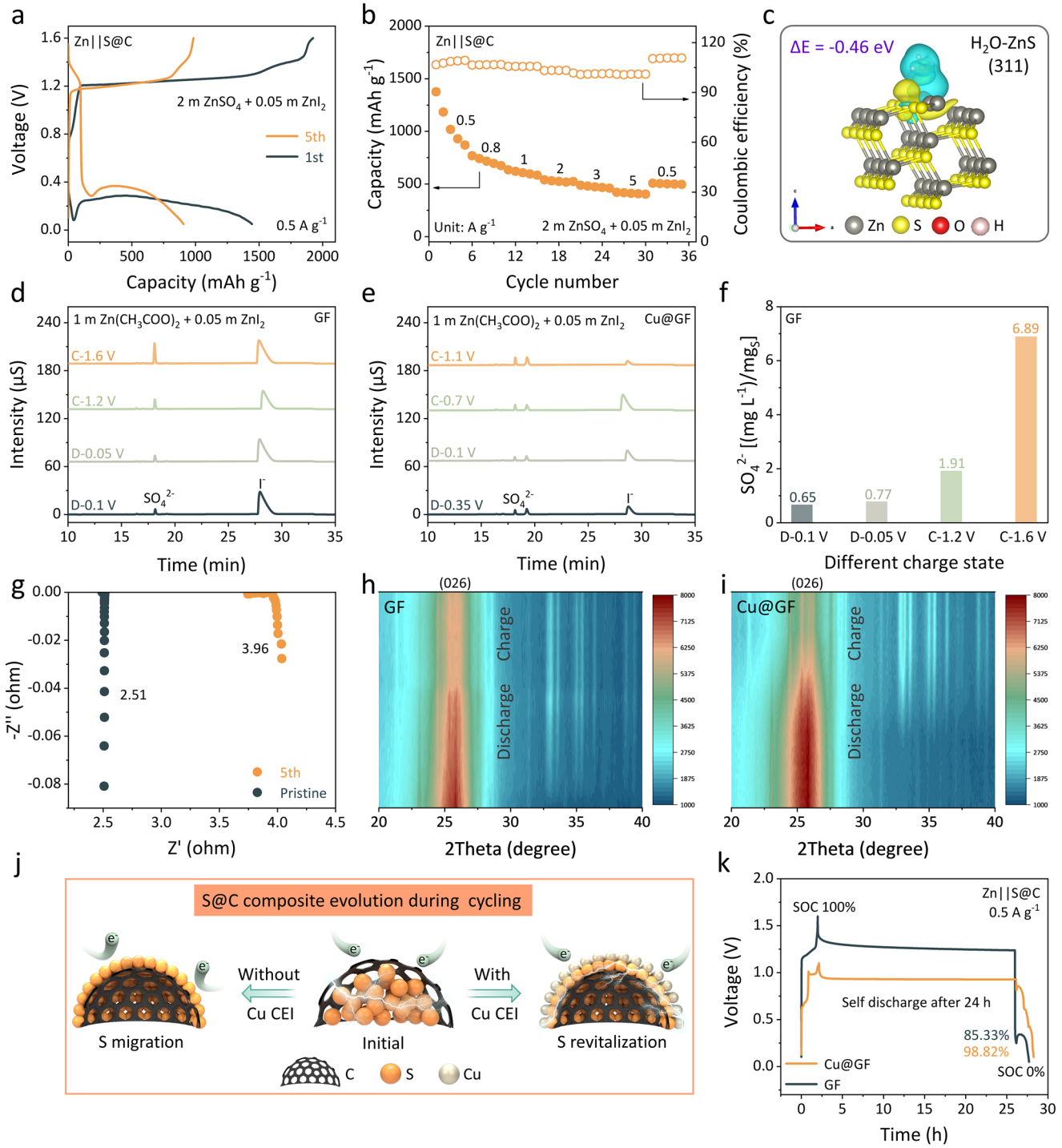

FIGURE 2 | Failure analysis of the aqueous Zn–S batteries. (a) Charge/discharge curves of Zn||S@C at 0.5 A g^{-1}. (b) Rate performances of Zn||S@C. (c) Charge density differences of H_2O-ZnS (311). Yellow and blue–green regions represent charge accumulation and depletion, respectively. IC results of the Zn–S batteries with (d) GF and (e) Cu@GF, and (f) the corresponding quantitative analysis with GF. The IC analysis was performed on the cycled sulfur cathode, separator and Zn anode using an electrolyte of 1 m $Zn(CH_3COO)_2$ + 0.05 m ZnI_2. Figures 2d and 2e show stacked Y-axis plots with the same intensity range. The absolute values do not represent actual signal strengths; only relative peak intensities are compared. (g) EIS results of the sulfur electrode before and after 5 cycles. In situ XRD results of the Zn–S batteries with (h) GF and (i) Cu@GF. (j) Schematic illustration of active sulfur leakage from the carbon host during cycling. (k) Self-discharge test results of Zn||S@C at 0.5 A g^{-1}.

tion remains inevitable during long-term cycling, the strong atom-level interaction between sulfur species and the conductive Cu CEI effectively reactivates otherwise insulating S_8 (Figure 2j), enabling its continued participation in subsequent redox reactions. As a result, the Zn||S@C cell employing the Cu@GF separator exhibits an outstanding capacity retention of 98.82% after a 24 h self-discharge test, substantially outperforming the GF-based counterpart (Figure 2k).

2.2 | Charge Storage Mechanism of Zn–S Batteries

To further elucidate the reaction mechanism, the role of the Cu CEI in regulating the Zn–S reaction pathway was investigated by tracking the structural evolution of S and Cu at different electrochemical stages. As depicted in Figure 3b, the sharp characteristic diffraction peaks of crystalline S_8 observed in the pristine S@C electrode (stage A) are largely masked by the carbon cloth substrate (Figure S1a), with only weak and inconspicuous reflections near ~26°. During the initial discharge of the Zn||S@C cell employing a bare GF separator (Figure 3a, stage A to D), broad diffraction peaks emerge at ~28.6°, ~33.1°, ~47.5°, and ~56.3°, which can be unambiguously assigned to the formation of crystalline ZnS (JCPDS no. 05–0566). This observation confirms that the dominant thermodynamic pathway involves the rapid reaction between S^{2-} and Zn^{2+} to form ZnS (Equation 2). Upon charging from stage D to G, the ZnS diffraction peaks gradually weaken and eventually disappear, while the characteristic reflections of S_8 reappear and intensify, indicating the effective oxidation of ZnS and regeneration of S_8 facilitated by the high concentration of I^- in the electrolyte. However, three-dimensional (3D) ion mapping reveals that, after cycling, sulfur species (S^+ signals) become heterogeneously distributed and lose intimate contact with the conductive carbon framework (Figures 3f and S22). This behavior is accompanied by substantial accumulation of sulfate species (SO_4^{2-}, SO^+ signals), demonstrating that although the I^- mediator enhances ZnS oxidation kinetics, it fails to suppress active sulfur migration and water-induced ZnS decomposition.

In contrast, when the Cu CEI is introduced, distinct mechanistic features emerge. During discharging (Figure 3c), the appearance of new diffraction peaks at ~25.5°, ~29.3°, ~42.2°, ~49.9°, and ~52.4° (Figure 3d, stage B), confirms the formation of CuI (JCPDS no. 06–0246). This result implies that I^- rapidly interacts with the Cu mediator following S_8 activation (Figure S23), a conclusion further corroborated by the suppressed I^- signal intensity observed in ion chromatography (IC) at the early discharge stage (Figure 2e). As discharge proceeds from stage B to D, the CuI diffraction signals diminish, while the corresponding I^- peak intensity in the ion chromatogram increases, reflecting the reduction of CuI to metallic Cu (JCPDS no. 04–0836) under continuous electron flux (Equation 4) [40, 41]. Meanwhile, the accompanying growth of ZnS diffraction peaks confirms sustained sulfur reduction facilitated by the Cu/CuI evolution. Additionally, the charge density difference plot in Figure 3h displays a high Cu-S_8 binding energy of −2.47 eV and the significant charge accumulation between Cu and S_8, suggesting the electron transfer from Cu to S_8 that facilitates S—S bond dissociation. Bond elongation generally reflects a reduction in bond dissociation energy, thereby promoting bond cleavage and sulfur reduction. Consistently, the calculated S—S bond length in S_8 elongates from 2.06 to 2.10 Å upon interaction with Cu. Similarly, adsorption of I^- on the S_8 surface also induces S—S bond elongation (Figure 3j).

During charging (stages D to G), the gradual intensification of CuI diffraction peaks coincides with the ZnS → S_8 conversion (Figure 3d), indicating a reversible ZnS oxidation pathway mediated by the transformation of Cu to CuI. Notably, extremely high lattice energy of ZnS (3400 kJ mol^{-1}) presents a substantial kinetic barrier for Zn–S covalent bond cleavage, thereby severely limiting its intrinsic conversion rate [42]. The strong adsorption affinities of both Cu and I^- toward ZnS (Figure 3h,j), together with the increased I^- signal observed in IC at the early charging stage, imply preferential binding of Cu and I^- to ZnS. This interaction induces Zn—S bond elongations of 3.8% and 6.4%, respectively. More importantly, electronic structure analysis reveals that adsorption of Cu and I^- shifts the Zn 3d-band center of the ZnS (311) surface from −6.19 eV to −6.09 eV and −6.04 eV, respectively (Figures 3i,k and S24), moving it closer to the Fermi level. This shift indicates surface electronic reconstruction and an increase in electron density around Zn atoms, which enhances Zn—S antibonding interactions and weakens the Zn—S covalent bond. The characteristic S-S vibrational modes of S_8 disappear upon full discharge (D-0.1 V) in ex situ Raman spectroscopy (Figure 3e), concomitant with the emergence of Zn–S vibrational signals corresponding to ZnS. Upon full charging (C-1.1 V), these spectral features are completely reversed. Furthermore, 3D ion mapping further confirms that the cycled active sulfur species remain homogeneously distributed between the conductive carbon network and the Cu CEI (Figures 3g and S25), preserving effective electrical contact. Simultaneously, the near absence of surface SO_4^{2-} firmly confirms the dual functionality of the Cu CEI in accelerating sulfur redox kinetics and stabilizing ZnS against aqueous corrosion.

$$2CuI(s) + Zn^{2+}(aq) + 2e^- \rightarrow 2Cu(s) + 2I^-(aq) + Zn^{2+}(aq),\ \Delta G = 35.73\ kJ\ mol^{-1} > 0 \quad (4)$$

$$ZnS(s) + Cu(s) + I^-(aq) - 3e^- \rightarrow S(s) + CuI(s) + Zn^{2+}(aq),\ \Delta G = 36.23\ kJ\ mol^{-1} > 0 \quad (5)$$

Based on these findings, the Cu CEI-enhanced Zn–S redox mechanism is schematically illustrated in Figure 3l. During discharging, the strong Cu-S_8 interaction drives spontaneous electron transfer from Cu to S_8, facilitating S—S bond dissociation and promoting S_8 ring opening and reduction to S^{2-}, which subsequently reacts with Zn^{2+} to form ZnS. In parallel, the transient Cu oxidation is buffered by iodide via reversible CuI formation, thereby ensuring sustained catalytic activity of the Cu CEI. During charging, both Cu and I^- strongly adsorb onto ZnS, significantly weakening Zn—S bonds and lowering the lattice energy of ZnS. This interaction induces partial structural disorder, triggering a domino-like oxidation of ZnS. Owing to the high affinity between Cu and S, a portion of ZnS may undergo transient conversion into copper sulfide species (e.g., Cu_2S) at the interface. Upon completion of charging, both ZnS and Cu_2S are fully oxidized to elemental S (Equation 5). Notably, the rapid regeneration of CuI at the end of charge indicates that the Cu-based CEI adaptively maintains a stable, highly reversible sulfur redox cycle through dynamic Cu/CuI interconversion (Figures S26 and S27).

2.3 | Electrochemical Performances of Zn||S@C Batteries

Remarkably, the Zn||S@C equipped with the Cu CEI exhibits markedly enhanced rate capability. As shown in Figure 4a, high

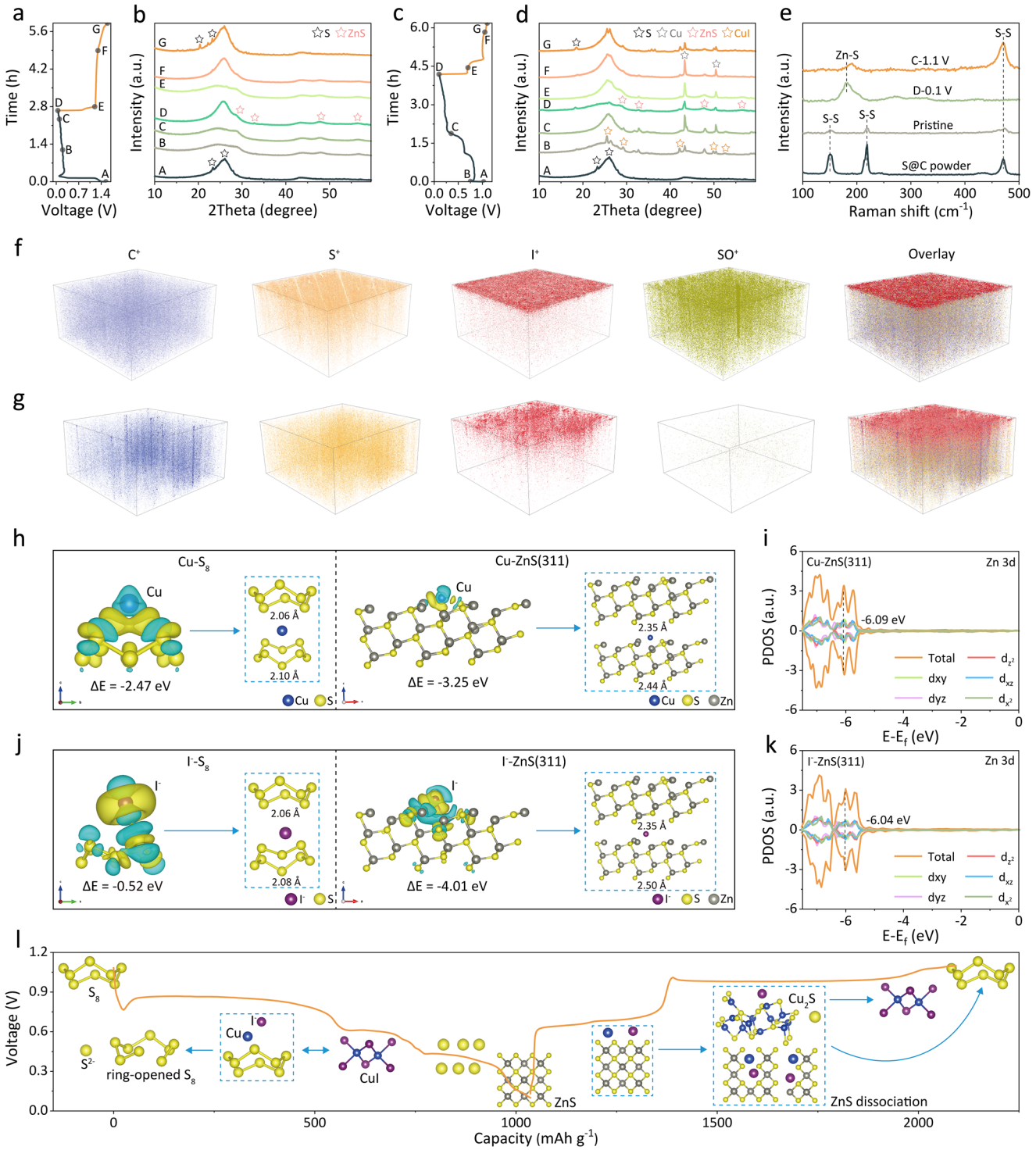

FIGURE 3 | Redox mechanism of Zn||S@C battery. Initial charge/discharge profiles of Zn||S@C batteries with (a) GF and (c) Cu@GF at 0.5 A g^{-1}, and (b,d) the corresponding ex situ XRD results of S@C cathode and Cu CEI. (e) Ex situ Raman results of S@C electrode with Cu@GF during the initial cycle. Time-of-flight secondary ion mass spectrometry (TOF-SIMS) analysis of the S@C electrodes after 5 cycles at 0.5 A g^{-1} in an electrolyte containing 1 m $Zn(CH_3COO)_2$ and 0.05 m ZnI_2, with (f) GF and (g) Cu@GF separators. Charge density differences of (h) Cu-S_8 and Cu-ZnS (311) and (j) I^--S_8 and I^--ZnS (311). Yellow and blue–green regions represent charge accumulation and depletion, respectively. Partial density of state (PDOS) results of the Zn 3d orbital in ZnS (311) after interacting with (i) Cu and (k) I^-. (l) Mechanistic diagram of the enhancement of Cu CEI in promoting sulfur redox kinetics.

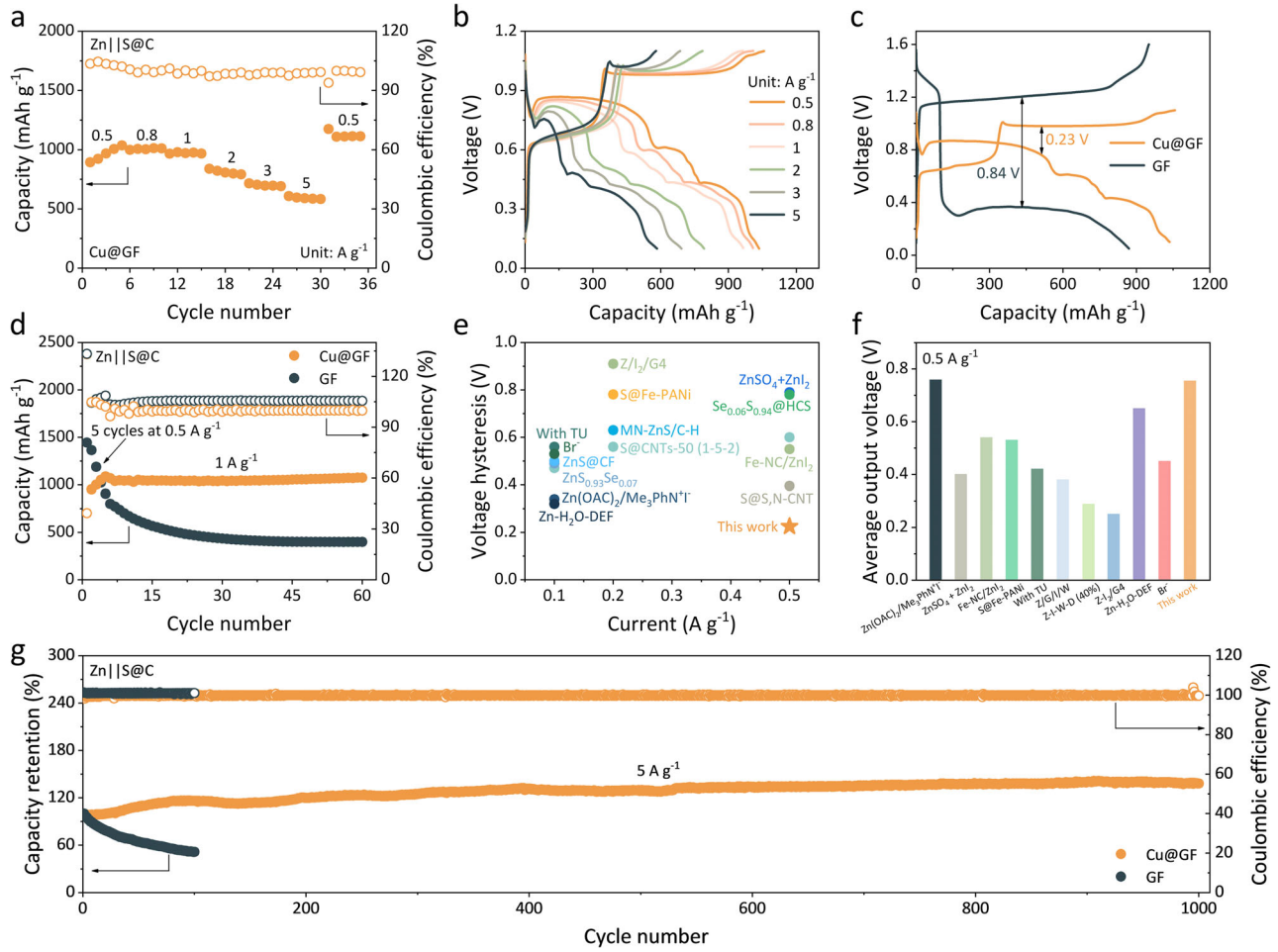

FIGURE 4 | Electrochemical performances of Zn||S@C batteries with Cu@GF. (a) Rate performance of Zn||S@C and (b) the corresponding charge/discharge profiles. (c) Charge/discharge profiles of Zn||S@C batteries with GF and Cu@GF at 0.5 A g^{-1}. Cycling performances of Zn||S@C batteries (d) at 1 and (g) 5 A g^{-1}. Comparisons of (e) voltage hysteresis and (f) average output voltage between the Zn||S@C with Cu@GF and the other reported Zn–S batteries.

capacity retentions of 97.59%, 93.42%, 76.47%, 66.81%, and 56.34% are achieved at current densities of 0.8, 1, 2, 3, and 5 A g^{-1}, respectively, relative to the capacity at 0.5 A g^{-1}. The corresponding charge-discharge profiles (Figure 4b) further reveal that the introduction of the Cu CEI significantly elevates the average discharge voltage of the sulfur cathode from below 0.4 to 0.75 V (Figure S28), while simultaneously reducing the voltage hysteresis from 0.84 to 0.23 V (Figure 4c). To the best of our knowledge, these values rank among the first echelon of previously reported aqueous Zn–S batteries (Figure 4e,f; Table S1 and S2) [4, 20, 21, 23, 27, 29–31, 37, 38, 43–48]. As presented in Figure 4d, the Zn||S@C cell with Cu CEI shows negligible capacity fade over 50 cycles at a moderate current density of 1 A g^{-1}, whereas its counterpart employing a bare GF separator undergoes rapid capacity fading. Additionally, the high conductive carbon content renders the sulfur cathode hydrophobic (electrolyte contact angle ~144.5°, Figure S29) [49], leading to an uneven I^- distribution and hindering ZnS oxidation. Fortunately, the hydrophilic Cu CEI (electrolyte contact angle ~25.3°) could not only ensure adequate electrolyte wetting at the interface between sulfur and Cu CEI, but also benefit from the efficient cooperation of I^- and Cu in improving the conversion reversibility of sulfur electrode (Figures S30 and S31). As a direct consequence of these synergistic interfacial and kinetic advantages, the Zn||S@C cell incorporating the Cu CEI demonstrates outstanding long-term durability, maintaining stable operation for 1000 cycles at a high current density of 5 A g^{-1} (Figure 4g).

Moreover, distribution of relaxation times (DRT) analysis derived from the in situ EIS (Figures S32 and S33) reveals that the introduction of Cu CEI significantly reduces the interfacial charge-transfer resistance (R_{ct}) of the sulfur cathode (Figure 5a,b). The relatively low R_{ct} during discharging reflects the accelerated S—S bond dissociation and ZnS formation, which can be attributed to the enhanced sulfur reduction kinetics and improved electrolyte wettability enabled by the Cu CEI with S affinity nature. In addition, the Cu CEI with ZnS affinity also promotes the oxidation of ZnS during charging, thereby facilitating Zn^{2+} transport within the sulfur electrode. This effect is evidenced by the reduced Warburg diffusion resistance (W_{diff}) during the charging process (Figure 5b). Based on the modified Arrhenius relationship of $1/R_{ct} = A\exp(-E_a/RT)$, the introduction of Cu CEI can significantly decrease the reaction activation energy of the Zn–S system from 69.4 to 29.5 kJ mol^{-1} (Figures 5d and S34). As a result, even at a high sulfur loading mass of ~3 mg cm^{-2} (Figure 5c), the Zn||S@C cell with Cu@GF can deliver a high areal capacity of ~2.6 mAh cm^{-2} for 50 cycles at

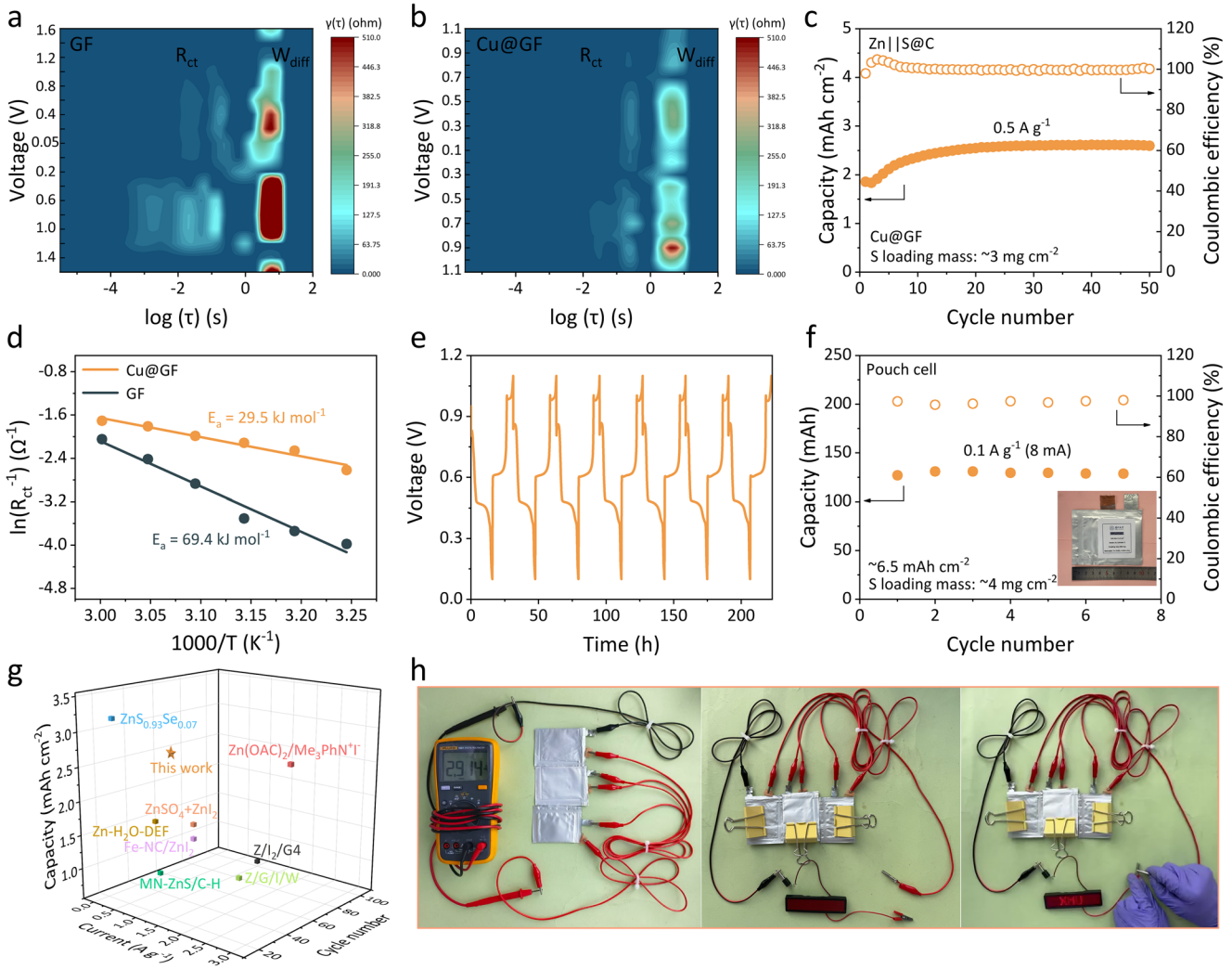

FIGURE 5 | Kinetic analysis and high-loading performance of Cu CEI-enabled Zn||S@C batteries. DRT results of Zn||S@C with (a) GF and (b) Cu@GF. (c) Cycling stability of Zn||S@C with Cu@GF at 0.5 A g^{-1}. (d) Arrhenius plots obtained from EIS spectra of Zn||S@C with GF/Cu@GF. (e) The voltage–time curves of Zn||S@C pouch cell with Cu@GF and (f) the corresponding cycling performance. (g) Comparisons of the electrochemical performances between Zn||S@C with Cu@GF and the other reported Zn–S batteries. (h) Photograph of the Zn||S@C pouch cell powering an LED panel.

0.5 A g^{-1}, outperforming many recently reported advanced Zn–S batteries (Figure 5g and Table S3) [4, 20, 23, 29, 31, 37, 43, 48]. The well-maintained shape of the differential capacity curves (Figure S35) also indicates that the robust Cu CEI effectively mitigates the key challenges under the high-loading conditions, such as sulfur leakage, incomplete ZnS oxidation, and active water attack, thereby advancing the development of practical Zn–S batteries. To further evaluate practical applicability, a Zn||S@C pouch cell (4 × 5 cm^2) incorporating the Cu CEI was assembled. The as-fabricated pouch cell delivers an impressive areal capacity of ~6.5 mAh cm^{-2} at an ultra-low rate of 0.1 A g^{-1} and maintains stable operation for more than 200 h (Figure 5e,f), demonstrating excellent durability under practical operating conditions. Compared with recently reported MnO_2, vanadium oxide, and MXene-based cathodes for aqueous zinc-based batteries, the Cu CEI-enabled Zn–S battery exhibits superior areal capacity at comparable active material loadings, particularly in a pouch cell configuration, underscoring its promise for high-energy-density energy storage (Table S4) [50–63]. Moreover, a series-connected pouch-cell module can power an LED panel (Figure 5h), providing a direct demonstration of the practical feasibility of the Cu CEI-enabled Zn–S battery system.

3 | Conclusion

In summary, the designed Cu CEI preferentially interacts with ZnS over water molecules, effectively suppressing ZnS decomposition into SO_4^{2-} and improving the cycling stability of Zn–S batteries, particularly at relatively low rates (<2 A g^{-1}). In addition, the strong intrinsic interactions of the Cu CEI with S_8 and ZnS significantly weaken the S—S and Zn—S bonds. In synergy with I^-, the activation energy of the Zn–S battery is substantially reduced from 69.4 to 29.5 kJ mol^{-1}. As a result, for the Zn–S battery with the sulfur/ZnS dual-affinity Cu CEI, the charge-discharge polarization is reduced from 0.84 to 0.23 V, and the average output voltage increases from below 0.4 to 0.75 V. More importantly, with a high loading mass of ~3 mg cm^{-2}, the Zn–S cell delivers stable cycling performance for 50 cycles at 0.5 A

g^{-1}, with an areal capacity of ~2.6 mAh cm^{-2}. Furthermore, the Zn–S pouch cell also maintains ~6.5 mAh cm^{-2} for over 200 h at a lower rate of 0.1 A g^{-1}, demonstrating that Cu CEI endows Zn–S batteries with excellent long-term stability under practical conditions.

Author Contributions

Zeheng Lv: conceptualization, investigation, validation, writing – original draft. **Peiyao Wang**: methodology, formal analysis. **Sirui Lin**: methodology, validation, investigation. **Xinran Li**: formal analysis and data curation. **Ruibo Sun**: visualization and validation. **Kaiwen Li**: investigation and visualization, **Hong Lin**: investigation, formal analysis, software. **Fanxiang Meng**: software, data curation, visualization. **Minghao Zhang**: validation and formal analysis. **Yang Yang**: writing – review editing and project administration, **Hao Luo**: resources, writing – review and editing. **Jinbao Zhao**: writing – review editing, funding acquisition, and supervision. **Dongliang Chao**: supervision, writing – review and editing.

Acknowledgments

The authors gratefully acknowledge the financial support from National Natural Science Foundation of China (Nos. 22579141, 22379125 and 22509170), Fundamental Research Funds for the Central Universities (20720250114) and the Natural Science Foundation of Fujian Province (No. 2024J011210).

Conflicts of Interest

The authors declare no conflicts of interest.

Data Availability Statement

The data that supports the findings of this study are available in the Supporting Information of this article.

References

1. H. Shahali, R. Sellers, A. Rafieerad, A. A. Polycarpou, and A. Amiri, "Progress and Prospects of Zinc-Sulfur Batteries," *Energy Storage Mater* 65 (2024): 103130, https://doi.org/10.1016/j.ensm.2023.103130.

2. H. Luo, F. Li, M. Wang, et al., "Reconstructing the Phase of Vanadium Oxides Enables Redox-Catalysis Manipulated Reversible Sulfur Conversion for Stable Zn–S Batteries," *Chemical Science* 16 (2025): 753–760, https://doi.org/10.1039/D4SC06593J.

3. X. Su, S. Li, Z. Chen, et al., "Steering $Zn(ClO_4)_2$ Electrolyte: Trifunctional Polycationic Artificial Interphase for Wide-Temperature Ah-Level Zn-I2 Pouch Cells," *Energy Storage Mater* 85 (2026): 104900, https://doi.org/10.1016/j.ensm.2026.104900.

4. W. L. Wu, S. B. Wang, L. Lin, H. Y. Shi, and X. Q. Sun, "A Dual-Mediator for a Sulfur Cathode Approaching Theoretical Capacity With Low Overpotential in Aqueous Zn–S Batteries," *Energy & Environmental Science* 16 (2023): 4326–4333, https://doi.org/10.1039/D3EE01749D.

5. T. Jiang, D. Shen, Z. Zhang, et al., "Battery Technologies for Grid-Scale Energy Storage," *Nature Reviews Clean Technology* 1 (2025): 474–492, https://doi.org/10.1038/s44359-025-00067-9.

6. R. Sinha, X. S. Xie, Y. Yang, et al., "Failure Mechanisms and Strategies for Vanadium Oxide-Based Cathode in Aqueous Zinc Batteries," *Advanced Energy Materials* 15 (2025): 2404815, https://doi.org/10.1002/aenm.202404815.

7. J. S. Cha, S. Park, N.-U. Seo, Y.-C. Kang, C.-W. Lee, and J. H. Yang, "Zincophilic CuO as Electron Sponge to Facilitate Dendrite-Free Zinc-Based Flow Battery," *Nature Communications* 16 (2025): 844, https://doi.org/10.1038/s41467-025-56011-9.

8. N. Zhang, X. Chen, M. Yu, Z. Niu, F. Cheng, and J. Chen, "Materials Chemistry for Rechargeable Zinc-Ion Batteries," *Chemical Society Reviews* 49 (2020): 4203–4219, https://doi.org/10.1039/C9CS00349E.

9. J. Wei, P. B. Zhang, J. J. Sun, et al., "Advanced Electrolytes for High-Performance Aqueous Zinc-Ion Batteries," *Chemical Society Reviews* 53 (2024): 10335–10369, https://doi.org/10.1039/D4CS00584H.

10. M. Tang, Q. Liu, X. Zou, B. Zhang, and L. An, "High-Energy-Density Aqueous Zinc-Ion Batteries: Recent Progress, Design Strategies, Challenges, and Perspectives," *Advanced Materials* 37 (2025): 2501361, https://doi.org/10.1002/adma.202501361.

11. X. H. Chen, X. F. Xie, P. C. Ruan, S. Q. Liang, W. Y. Wong, and G. Z. Fang, "Thermodynamics and Kinetics of Conversion Reaction in Zinc Batteries," *ACS Energy Letters* 9 (2024): 2037–2056, https://doi.org/10.1021/acsenergylett.4c00450.

12. W. Q. Yao, K. Liao, T. X. Lai, H. Sul, and A. Manthiram, "Rechargeable Metal-Sulfur Batteries: Key Materials to Mechanisms," *Chemical Reviews* 124 (2024): 4935–5118, https://doi.org/10.1021/acs.chemrev.3c00919.

13. T. S. Zhang, Y. L. Zhao, Y. T. Feng, et al., "Aqueous-S vs Organic-S Battery: Volmer-Step Involved Sulfur Reaction," *Journal of the American Chemical Society* 147 (2025): 11501–11510, https://doi.org/10.1021/jacs.5c01727.

14. J. H. Liu, W. H. Zhou, R. Z. Zhao, et al., "Sulfur-Based Aqueous Batteries: Electrochemistry and Strategies," *Journal of the American Chemical Society* 143 (2021): 15475–15489, https://doi.org/10.1021/jacs.1c06923.

15. J. H. Liu, C. Ye, H. Wu, M. Jaroniec, and S. Z. Qiao, "2D Mesoporous Zincophilic Sieve for High-Rate Sulfur-Based Aqueous Zinc Batteries," *Journal of the American Chemical Society* 145 (2023): 5384–5392, https://doi.org/10.1021/jacs.2c13540.

16. Y. T. Feng, B. Y. Wang, W. H. Zhou, et al., "High-Valent Thiosulfate Redox Electrochemistry for Advanced Sulfur-Based Aqueous Batteries," *Journal of the American Chemical Society* 146 (2024): 25343–25349, https://doi.org/10.1021/jacs.4c10159.

17. H. Luo, X. Su, Z. Chen, et al., "Aqueous Iron-Ions Batteries: Status, Solutions, and Prospects," *Advanced Materials* 37 (2025): 2507978, https://doi.org/10.1002/adma.202507978.

18. H. Luo, H. Guo, X. Li, et al., "Aqueous manganese-ion batteries: The past, present, and future," *Matter* 8 (2025): 102379 https://doi.org/10.1016/j.matt.2025.102379

19. S. Shen, C. Yuan, Y. Xu, et al., "Improving ZnS Oxidation Kinetics Through Nucleophilic Regulation for High-Performance Zinc–Sulfur Batteries," *Advanced Functional Materials* 35 (2025): 2420258, https://doi.org/10.1002/adfm.202420258.

20. H. Li, M. Zhang, Z. Zheng, et al., "High-Capacity and Long-Life Aqueous Zn-SPAN Batteries With Tandem Catalysis," *Advanced Materials* 37 (2025): 2409771, https://doi.org/10.1002/adma.202409771.

21. D. Liu, B. He, Y. Zhong, et al., "A Durable ZnS Cathode for Aqueous Zn-S Batteries," *Nano Energy* 101 (2022): 107474, https://doi.org/10.1016/j.nanoen.2022.107474.

22. W. Li, K. Wang, and K. Jiang, "A Low Cost Aqueous Zn–S Battery RealizingUltrahigh Energy Density," *Advancement of Science* 7 (2020): 2000761 https://doi.org/10.1002/advs.202000761.

23. P. Hei, Y. Sai, C. Liu, et al., "Facilitating the Electrochemical Oxidation of ZnS Through Iodide Catalysis for Aqueous Zinc-Sulfur Batteries," *Angewandte Chemie International Edition* 63 (2024): e202316082, https://doi.org/10.1002/anie.202316082.

24. J. Liu, Y. Chen, H. Wu, C. Ye, and S. Z. Qiao, "Anti-Corrosive Covalent Iodo-Thiadiazole Catalyst Enables Aqueous Zn—S Batteries With High Coulombic Efficiency," *Advanced Materials* 37 (2025): e08570, https://doi.org/10.1002/adma.202508570.

25. G. Chang, J. Liu, Y. Hao, et al., "Bifunctional Electrolyte Additive With Redox Mediation and Capacity Contribution for Sulfur Cathode in Aqueous Zn-S Batteries," *Chemical Engineering Journal* 457 (2023): 141083, https://doi.org/10.1016/j.cej.2022.141083.

26. J. Liu, H. Wu, C. Ye, and S. Z. Qiao, "High-Entropy Sulfides Catalyze Rate-DeterminingRedox in Fast-Charging Aqueous Zinc–Sulfur Batteries," *Angewandte Chemie International Edition* 64 (2025): e202503472 https://doi.org/10.1002/anie.202503472.

27. S. Wang, W. Wu, Q. Jiang, et al., "Uncovering ZnS Growth Behavior and Morphology Control for High-Performance Aqueous Zn–S Batteries," *Chemical Science* 16 (2025): 1802–1808, https://doi.org/10.1039/D4SC07285E.

28. L. W. Luo, C. Zhang, X. Y. Wu, et al., "A Zn–S Aqueous Primary Battery With High Energy and Flat Discharge Plateau," *Chemical Communications* 57 (2021): 9918–9921, https://doi.org/10.1039/D1CC04337D.

29. P. Hei, Y. Sai, L. Yu, et al., "Cosolvent Electrolyte Design for High-Voltage Aqueous Zinc–Sulfur Batteries," *Journal of the American Chemical Society* 147 (2025): 27802–27811, https://doi.org/10.1021/jacs.5c06710.

30. H. Zhang, Z. Shang, G. Luo, et al., "Redox Catalysis Promoted Activation of Sulfur Redox Chemistry for Energy-Dense Flexible Solid-State Zn–S Battery," *ACS Nano* 16 (2021): 7344–7351, https://doi.org/10.1021/acsnano.1c08645.

31. P. Dai, J. Lang, W. Huang, et al., "Spin State Modulation via Magnetic Fields in Fe Single Atom Catalysts for High-Performance Aqueous Zinc–Sulfur Batteries," *ACS Nano* 19 (2025): 21083–21094, https://doi.org/10.1021/acsnano.5c05185.

32. H. Guo, H. Luo, F. Zhu, et al., "Mechanical-Thermal Decoupling Engineering Unlocks Ultra-Stable Dry Thick Iodine Cathodes for Ah-Level Zinc-Based Pouch Batteries," *Advanced Materials* 38 (2026): e73037, https://doi.org/10.1002/adma.73037.

33. Y. Guo, X. Zhu, J. Zhang, et al., "Engineering Electrolyte Network Structure for Improved Kinetics andDendrite Suppression in Zn-S Batteries," *Angewandte Chemie International Edition* 64 (2025): e202422047, https://doi.org/10.1002/anie.202422047.

34. M. K. Denk, "The Variable Strength of the Sulfur–Sulfur Bond: 78 to 41 Kcal—G3, CBS-Q, and DFT Bond Energies of Sulfur (S_8) and Disulfanes XSSX (X = H, F, Cl, CH_3, CN, NH_2, OH, SH)," *European Journal of Inorganic Chemistry* 2009 (2009): 1358–1368, https://doi.org/10.1002/ejic.200800880.

35. Y. Luo, W. Sun, H. Han, J. Peng, and F. Jiang, "Uncovering the Oxidation Mechanism of Sphalerite (ZnS) in the Absence and Presence of Water: A First-Principles Investigation," *International Journal of Mining Science and Technology* 35 (2025): 149–157, https://doi.org/10.1016/j.ijmst.2024.12.004.

36. P. Paydary and P. Larese-Casanova, "Water Chemistry Influences on Long-Term Dissolution Kinetics of CdSe/ZnS Quantum Dots," *Journal of Environmental Sciences* 90 (2020): 216–233, https://doi.org/10.1016/j.jes.2019.11.011.

37. M. Yang, Z. Yan, J. Xiao, et al., "Boosting Cathode Activity and Anode Stability of Zn-S Batteries in Aqueous Media Through Cosolvent-Catalyst Synergy," *Angewandte Chemie International Edition* 61 (2022): e202212666, https://doi.org/10.1002/anie.202212666.

38. D. Patel, A. Dharmesh, Y. Sharma, P. Rani, and A. K. Sharma, "Hybrid Electrolyte With Biomass-Derived Carbon Host for High-Performance Aqueous Zn–S Battery," *Chemical Engineering Journal* 479 (2024): 147722, https://doi.org/10.1016/j.cej.2023.147722.

39. T. Lu and F. Chen, "Bond Order Analysis Based on the Laplacian of Electron Density in Fuzzy Overlap Space," *Journal of Physical Chemistry A* 117 (2013): 3100–3108, https://doi.org/10.1021/jp4010345.

40. J. Hao, L. Yuan, B. Johannessen, et al., "Studying the Conversion Mechanism to Broaden Cathode Options in Aqueous Zinc-Ion Batteries," *Angewandte Chemie International Edition* 60 (2021): 25114–25121, https://doi.org/10.1002/anie.202111398.

41. W. Li and D. Wang, "Conversion-Type Cathode Materials for Aqueous Zn Metal Batteries in Nonalkaline Aqueous Electrolytes: Progress, Challenges, and Solutions," *Advanced Materials* 37 (2025): 2304983, https://doi.org/10.1002/adma.202304983.

42. P. Hei, G. Hu, L. Yu, et al., "Copper Sulfide Catalysts Facilitating Zinc Sulfide Electro-Oxidation in Aqueous Zinc–sulfur Batteries," *Chemical Engineering Journal* 525 (2025): 170373, https://doi.org/10.1016/j.cej.2025.170373.

43. M. Yang, Z. C. Yan, H. Zhang, et al., "Controllable Synthesis of Sub-10 Nm ZnS Nanograins Confined in Micro-Size Carbon Skeleton for Aqueous Zn–S Batteries," *Advanced Functional Materials* 34 (2024): 2406077, https://doi.org/10.1002/adfm.202406077.

44. H. Zhang, M. Yang, J. Xiao, et al., "Internal Electron Donor Accelerated Sulfur Redox for Aqueous Zn—S Batteries," *Advanced Functional Materials* 34 (2024): 2406125, https://doi.org/10.1002/adfm.202406125.

45. T. Zhou, H. Wan, M. Liu, Q. Wu, Z. Fan, and Y. Zhu, "Regulating Uniform Nucleation of ZnS Enables Low-Polarized and High Stable Aqueous Zn–S Batteries," *Mater Today Energy* 27 (2022): 101025, https://doi.org/10.1016/j.mtener.2022.101025.

46. J. Li, J. L. Liu, F. X. Xie, R. Bi, and L. Zhang, "Synergistic Electrocatalysis and Spatial Nanoconfinement to Accelerate Sulfur Conversion Kinetics in Aqueous Zn—S Battery," *Angewandte Chemie International Edition* 63 (2024): e202406126, https://doi.org/10.1002/anie.202406126.

47. J. Li, J. Cong, Y. Ren, H. Ji, Z. Li, and Y. Huang, "Constructing a Raincoat-Like Protective Layer on Sulfur Cathode for Aqueous Zn–S Batteries," *Energy Storage Mater* 70 (2024): 103541, https://doi.org/10.1016/j.ensm.2024.103541.

48. Y. B. Ren, J. B. Li, Y. Zhang, Y. H. Huang, and Z. Li, "Trace Selenium Doping forImproving the Reaction Kinetics of ZnS Cathode for Aqueous Zn–S Batteries," *Small* 20 (2024): 2402466, https://doi.org/10.1002/smll.202402466.

49. Y. Luo, S. Pan, J. Tian, et al., "Engineering Triple-Phase Interfaces With Hierarchical Carbon Nanocages for High-Areal-Capacity All-Solid-State Li-S Batteries," *Advanced Materials* 36 (2024): 2413325, https://doi.org/10.1002/adma.202413325.

50. A. Chen, D. Li, Q. Li, Z. Chen, Z. Huang, and C. Zhi, "Cathode materials for zinc-basedbatteries," *Nano Research Energy* 4 (2025): e9120204, https://doi.org/10.26599/NRE.2025.9120204.

51. J. Chen, Y. Zhao, X. Yang, L. Tan, X. Wu, and C. Chen, "Recent advances in MXene materialsfor zinc-ion hybrid capacitors," *Nano Research Energy* 4 (2025): e9120154 , https://doi.org/10.26599/NRE.2025.9120154.

52. R. Venkatkarthick, N. Rodthongkum, X. Zhang, et al., "Vanadium-Based Oxide on Two-Dimensional Vanadium Carbide MXene (V_2O_x@V_2CT_x) as Cathode for Rechargeable Aqueous Zinc-Ion Batteries," *ACS Applied Energy Materials* 3 (2020): 4677–4689, https://doi.org/10.1021/acsaem.0c00309.

53. G. Zhao, S. Meng, Z. Zheng, et al., "From Crystalline to Amorphous: V2CT MXene Cathodes Enable High-Capacity and Long-Life Aqueous Zinc Ion Batteries," *GreenChemical Engineering* (2025), https://doi.org/10.1016/j.gce.2025.12.001.

54. X. Zheng, B. Han, S. Cheng, S. Liu, F. Wang, and Y. Wu, "Molecular Armor Encapsulationof Practical Layered Cathode Empowers Energetic Ah-Level Zn-MnO2 Pouch andPrismatic Cells," *JACS Au* 5 (2025): 4904–4915, https://doi.org/10.1021/jacsau.5c00836.

55. M. Shi, B. Wang, C. Chen, J. Lang, C. Yan, and X. Yan, "3D high-Density MXene@MnO_2 Microflowers for Advanced Aqueous Zinc-Ion Batteries," *Journal of Materials Chemistry A* 8 (2020): 24635–24644, https://doi.org/10.1039/D0TA09085A.

56. X. Zhu, W. Wang, Z. Cao, et al., "Zn 2+ -Intercalated V_2O_5 nH_2O Derived From V_2CT_X MXene for Hyper-Stable Zinc-Ion Storage," *Journal of Materials Chemistry A* 9 (2021): 17994–18005, https://doi.org/10.1039/D1TA05526G.

57. T.-H. Wu, T.-K. Li, and L.-J. Guo, "Efficient Structural and Compositional Modulation of Vanadium Oxides for High-Areal-Capacity Zinc-Ion Batteries," *Journal of Power Sources* 623 (2024): 235503, https://doi.org/10.1016/j.jpowsour.2024.235503.

58. J. Wei, L. Tan, Q. Ma, et al., "Achieving Ah-Level Zn–MnO_2 Pouch Cells via Interfacial Solvation Structure Engineering," *Nano-Micro Lett* 18 (2026): 124, https://doi.org/10.1007/s40820-025-01935-6.

59. G. Lai, Z. Zhao, H. Zhang, et al., "In-Situ Positive Electrode-Electrolyte Interphase Construction Enables Stable Ah-Level Zn-MnO_2 Batteries," *Nature Communications* 16 (2025): 2194, https://doi.org/10.1038/s41467-025-57579-y.

60. M. Liu, X. Li, M. Cui, et al., "Amorphous Organic-Hybrid Vanadium Oxide for Near-Barrier-Free Ultrafast-Charging Aqueous Zinc-Ion Battery," *Nature Communications* 15 (2024): 10769, https://doi.org/10.1038/s41467-024-55000-8.

61. Y. Song, M. Chen, Z. Zhong, Z. Liu, S. Liang, and G. Fang, "Bilateral In-Situ Functionalization Towards Ah-Scale Aqueous Zinc Metal Batteries," *Nature Communications* 16 (2025): 3142, https://doi.org/10.1038/s41467-025-58153-2.

62. C. Yang, P. Woottapanit, S. Geng, et al., "A Multifunctional Quasi-Solid-State Polymer Electrolyte With Highly Selective Ion Highways for Practical Zinc Ion Batteries," *Nature Communications* 16 (2025): 183, https://doi.org/10.1038/s41467-024-55656-2.

63. H. Liu, J. Sun, P. Sun, et al., "Polyacrylic Acid Binder Enabling High Areal Capacity $V_2O_5nH_2O$ Cathode for Aqueous Zinc-Ion Batteries," *Small* 21 (2025): 2503069, https://doi.org/10.1002/smll.202503069.

Supporting Information

Additional supporting information can be found online in the Supporting Information section.

Supporting File: anie73206-sup-0001-SuppMat.docx.